

UNDERSTANDING THE DYNAMICS OF ULTRASONIC ADDITIVE MANUFACTURING

Qing Mao*, Nicole Coutris*, James Gibert†, Georges Fadel*

*Department of Mechanical Engineering, Clemson University, SC 29630

†Department of Mechanical Engineering, Purdue University, NY 13699

REVIEWED

Abstract

Ultrasonic Additive Manufacturing (UAM) is an additive manufacturing technique that uses ultrasound to merge metal foils (150 μm thick, 24 mm wide) layer by layer to fabricate three-dimensional bodies. As new layers are deposited and the height-to-width ratio of the built feature changes, the dynamics of UAM changes accordingly. Prior research suggested the existence of a limit for the height-to-width ratio. Above this limit, additional layers fail to bond because the built feature reaches its resonance frequency. Specifically, the bond failure is affected by the lack of plastic shear deformation between two foils which is essential to the generation of true metallic bonds. As the height-to-width ratio falls in the critical range, the built feature becomes resonant under the high-frequency excitations (20 kHz) of the sonotrode, leading to large-amplitude oscillations matching those of the sonotrode, and resulting in reduction of differential motion and therefore plastic shear deformation between the foils. In order to develop a model incorporating plasticity, heat transfer, and friction to study UAM, 2-D and 3-D lump parameter models consisting of mass-spring networks are proposed to study the dynamics of the elastic part of the built feature. The models are established such that they preserve the modal parameters of the built feature in free vibration. The lumped parameter models are validated by comparing their modal predictions with those from 2-D and 3-D finite element models. The lumped parameter model will be coupled with a 3-D finite element model to describe an elasto-plastic bonding layer introducing the friction and thermal aspects of UAM. By examining the deformation of the bonding layer under the combined effects of the excitation of the sonotrode and the vibration of the built feature, the bond failure due to geometry change of the built feature will be better understood and quantified in the future.

1. Introduction

The ultrasonic additive manufacturing (UAM) is a solid state fabrication process that joins metal foils (150 μm thick, 24 mm wide) layer by layer through ultrasonic metal welding and removes excessive materials using CNC contour milling. The welding process is realized by a sonotrode that vibrates (amplitude: 5 – 40 μm , frequency: 20 kHz) in transversal direction as shown in fig. 1 (a) and rolls (speed: 2.5 m/min) in longitudinal direction while being subjected to a moderate compressive force (1600 N) normal to bonding area. Its rough surface texture allows the sonotrode to “grab” the top foil and vibrate with respect to the built feature while the normal compression enables intimate contact between the foil and the built feature. As a result, true metallic bonds are generated under the combined effects of ultrasonic vibration and moderate compression (fig. 1 (b)). Specifically, the bond formation is generated following three stages (de

Vries, 2004). In the first stage, the surfaces to be welded are drawn together by moderate normal compression. The tips of asperities at the microscale are brought into contact and plastically deformed by the normal and shear stresses generated from normal compression and interfacial vibration respectively. Moreover, the shear stresses facilitate the break-up of hard surface oxides by deforming the softer pure metals beneath the oxides. In the second stage, the metal-to-metal contact area increases as plastic deformation proceeds. Meanwhile, the broken oxides are dispersed to the edge of the weld zone by the shear stresses, which generates a clean mating surface (Ram et al., 2007). In the third stage, a strong bond is formed through close contact of metals. The underlying bond mechanism is still arguable but could be one or a combination of the following: metallic adhesion, diffusion, localized melting, recrystallization, and mechanical interlock. Notice that the bonds are formed only in a contact patch underneath the sonotrode and between the top foil and the built feature at this point. As the sonotrode rolls forwards, the bonded area expands. The three stages during the bond formation take place within very short time intervals and are therefore hard to separate. It is clear that the interfacial ultrasonic vibration, normal compression, and rolling speed all play a role in the bond formation. However, the importance of interfacial ultrasonic vibration stands out as it generates shear stresses that govern the plastic deformation of materials, the break-up and dispersion of the surface oxides, and the delivery of the ultrasonic energy into the weld parts.

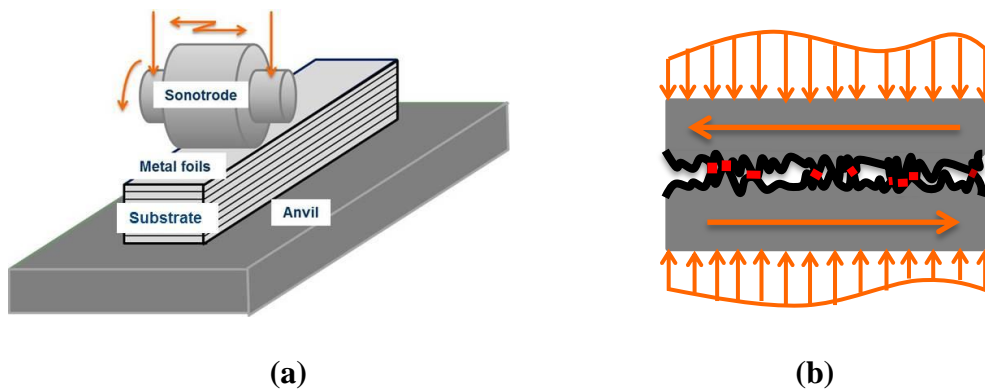


Fig.1 (a) The schematics of the ultrasonic additive manufacturing, (b) schematics of bonding

Despite the advantages of being able to join dissimilar materials, operate at relatively low temperature (300 °F or 150 °C) and thus inducing lower thermal residual stresses than many other additive manufacturing techniques, UAM has not established itself as an attractive manufacturing alternatives probably because of a critical operational issue known as “height-to-width ratio problem”(Robinson et al., 2006). Specifically, as the height of the built feature approaches its width, bonding failure occurs between the top foil and the built feature and additional layers cannot be bonded. The issue is observed to be independent of the length of the feature. In aluminum 3003-H18, the bond failure is observed as the height-to-width ratio falls in the range of 0.7 to 1.2. Many researchers investigated the issue and reached a uniform conclusion that the bond degradation is due to insufficient differential motion between the foil and the built feature, although their interpretation of the conclusion varies significantly. The loss of differential motion leads to a lack of shear stresses which is believed to be a critical factor in bond formation. In order to better describe the bond region by taking into account of plasticity, friction, and heat transfer aspects, lumped parameter models consisting of mass-spring networks

are proposed to study the elastic deformation of the built feature and therefore to characterize the reduction of the differential motion in UAM. The models are shown to be capable to accurately predict the modal parameters of the built feature and require lower mesh resolution than the finite element model.

2. Literature Review

In the investigation of the height-to-width bond failure issue, researchers proposed different theories to interpret the loss of differential motion that leads to bond failure. Robinson et al. (Robinson et al., 2006) investigated the influence of the built feature geometry on its stiffness by building a series of free-standing rib structures with varying dimensions and orientations. They found that the bond failure is due to the feature's lack of stiffness with respect to the sonotrode vibration direction as the height to width ratio of the built feature approaches 1:1. The lack of stiffness results in excessive deflection of the built feature that further leads to a reduction and eventual elimination of the differential motion between the top foil and the substrate and consequently a lack of plastic deformation necessary to bond formation. Zhang and Li (Zhang and Li, 2006) developed a 2-D finite element model in which they considered the plane perpendicular to the welding direction passing through the center of the sonotrode. They studied the contact frictional stresses and interfacial displacement between the foils and the built feature and observed a decrease in both as the height-to-width ratio approaches the critical value 1. They associated the decrease of both interfacial displacement and friction to the superposition of traveling vibrational waves within the built feature which produces a minimum displacement at the bonding interface (Zhang et al., 2006). However, the superposition theory indicates that bond failure is associated with a critical height rather than a critical height-to-width ratio. Gibert et al. (Gibert et al., 2009) investigated the vibration of the built features at various high-to-width ratios: 0.5, 1.0 and 2.0. They found that bonding can be re-initiated beyond the critical height-to-width ratio, meaning that the lack of stiffness proposed by Robinson et al. is not sufficient to account for the reduction of differential motion. By using a Rayleigh-Ritz model, they showed that an increase in height to width ratio causes several natural frequencies of the built feature to approach the 20 kHz excitation frequency of the sonotrode (Gibert et al., 2009). In addition, they developed a 3-D finite element model and a 2-D lumped parameter model to show a substantial decrease of differential motions due to resonance as the height-to-width ratio approaches critical values. As a result, Gibert et al. proposed that the resonance of the built feature is excited at the critical height-to-width ratio, resulting in large amplitude transversal vibration of the built feature that counteracts with vibration of the sonotrode. In this paper, the role of resonance in the reduction of differential motion at the critical height-to-width ratio is studied. Therefore, a dynamic model able to capture the natural frequencies and mode shapes of the built feature at critical height-to-width ratio is needed.

Different dynamic models have been proposed to characterize the dynamics of the built feature. The most extensively adopted models are finite element models. Zhang et al. (Zhang et al., 2006) developed a 2-D finite element model and applied transient dynamics analysis using the commercial software package ANSYS. However, the 2-D model provides only an approximation of the primary modal frequency and mode shape of the 3-D case. As the modal number increases, the prediction from the 2-D case diverges from the 3-D case. This is due to the weakening of the assumption of plane strain about the cross section as the mode shapes become

complicated at higher order (Cosby et al., 2013). Gibert et al. (Gibert et al., 2009) established a 3-D finite element model for the built feature and performed a preliminary dynamic transient analysis using the commercial software ABAQUS Explicit. Due to the high frequency characteristics, the analysis is computationally expensive. Simulations are run for only 2 milliseconds (40 cycles), which is not sufficient for an impulsive load to die out or for the foil to undergo plastic deformation (Gibert et al., 2009). As a result, a simpler and less computationally demanding dynamic model is required.

A mass spring system is intuitive and simple in representing a continuum in which matter is discretized into mass particles that are linked by massless linear springs. The system was first implemented to represent the elasticity and dynamical theory of Crystal Lattices (Born and Ann, 1914; Born, 1954), and later the mass-spring system was used in computer graphics (Nealen et al., 2006) to model the isotropic and anisotropic behaviors of materials. The system has a straight forward concept: the state of the system is defined by the displacement \mathbf{x} of the particles i which possesses a mass m_i . The motion of each particle is governed by Newton's second law: $f_i = m_i \ddot{\mathbf{x}}_i$. The force f_i is the sum of external forces (friction, gravity, etc.) and internal forces exerted by the springs, and $\ddot{\mathbf{x}}_i$ is the acceleration of the particle i . The gravity is small compared with internal forces and is therefore ignored. Under the assumption that the continuum undergoes elastic deformation, the internal forces between particle i and j , $f_{in,ij}$, are calculated based on the Hooke's law: $f_{in,ij} = \sum k_{ij}(\mathbf{x}_i - \mathbf{x}_j)$, where k_{ij} is the stiffness constant of the spring that connects particles i and j , and is governed by the configurations of the springs and the directional dependence of material's mechanical properties (isotropic or anisotropic). The spring stiffness can be determined either by finding optimal parameters that match the measured deformation data or from analytical expressions. The data-driven approach can be found in work by San-Vicente et al. (San-Vicente, 2012), and Louchet et al. (Louchet et al., 1995). The analytical approach can be found in work by Baudet et al. (Baudet et al, 2009), and Ladd et al. (Ladd et al., 1997). The data-driven approach may experience convergence issues, converge to zero, or result in negative spring stiffnesses (Lloyd et al., 2007). The analytical approach provides more realistic spring stiffnesses based on the elasticity and dynamical theory of the discrete model. However, its application is limited by the over simplified structure of the model. The detailed explanation is presented in sections 3 and 4. In this paper, the analytical approach is used for determining spring stiffness. The prediction from the mass-spring model depends on the mesh resolution and spring configuration. In some cases, if the model requires too high a mesh resolution it may undermine the primary goal of using the mass-spring system. As a result, the established mass-spring system should be evaluated in terms of effectiveness and computational efficiency.

3. 2-D Mass-spring Models

First we establish a 2-D model with assumptions similar to those for the 2-D model of Zhang et al. (Zhang et al, 2010). The domain is normal to the bonding interface and aligned with the direction of the ultrasonic vibration. In this plane, plane strain conditions can be assumed. In establishing the mass-spring model, we determine first the shape and spring configurations of the unit cell. The possible shapes of the unit cell include rectangular, triangular, and hexagonal shapes. Since the built feature is a parallelepiped and its cross section is rectangular, it is intuitive and convenient to select rectangular unit cells. Then a rectangular unit cell with the simplest

spring configuration consisting of four edge springs is evaluated based on tensile and shearing tests. It is obvious that the edge springs of the square cell are capable of capturing the tensile deformation but fail the shearing tests. Since the rectangular cell is not constrained by torsional springs at the vertices, the structure can deform freely in the shearing tests without deforming any of the edge springs (fig. 2 (a)). As a result, two diagonal springs are introduced to account for the shearing effects (fig. 2 (b)). The two diagonal springs have equal stiffness coefficients. The spring constants for both the edge and the diagonal springs are derived based on tensile and shearing tests of actual physical models presented by Baudet et al. (Baudet et al, 2009). Based on energy method, the relations between the internal forces and deformations are established and elastic parameters (Young's modulus and Poisson's ratio) can be introduced. As only diagonal springs are stressed in small shear deformation, the spring constants of edge springs k_i and diagonal springs k_d are easily obtained:

$$k_i = \frac{E(j^2(3\nu + 2) - i^2)}{4x_0y_0(1 + \nu)}, \quad (i, j) \in \{x_0, y_0\}^2 \text{ with } i \neq j \quad (1)$$

$$k_d = \frac{E(x_0^2 + y_0^2)}{4x_0y_0(1 + \nu)} \quad (2)$$

Where x_0 and y_0 represents the width and height of the unit cell. In this paper, square unit cells are implemented for their simplicity and effectiveness: $x_0 = y_0$. E is the Young's modulus, and ν is the Poisson's ratio. Kot et al. (Kot et al., 2014) provided a comprehensive demonstration of a limitation of the model showing that for any particle models with central forces (the spring forces depend only on the distance between masses), Poisson's ratios in 2-D and 3-D can always be written:

$$v_{2D} = \frac{\lambda}{\lambda + 2\mu} \quad (3)$$

$$v_{3D} = \frac{\lambda}{2(\lambda + \mu)} \quad (4)$$

Where λ and μ are the Lamé constants. For an isotropic solid, $\lambda = \mu$ holds for the central force models (Rice, 1993), and equation (3) and (4) become:

$$v_{2D} = 1/3$$

$$v_{3D} = 1/4$$

Therefore the mass-spring system provides exact prediction only for materials with Poisson's ratio $v_{2D} = 1/3$ in 2-D case and $v_{3D} = 1/4$ in 3-D case. However, by introducing some corrective forces, any different Poisson's ratio can be used (Baudet et al., 2009). The aluminum 3003-H18 has a Poisson's ratio of 1/3 and thus can be modeled using 2-D mass spring model. For the 3-D case, additional modification is required to adapt the model for the assigned material.

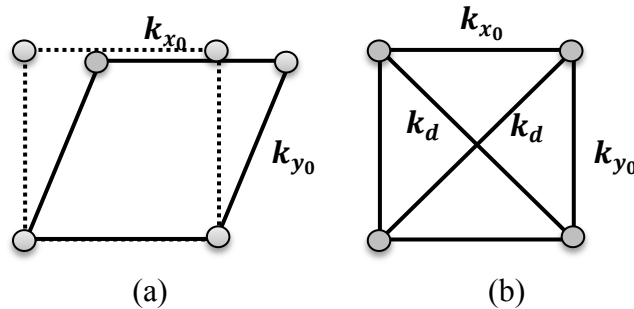


Fig.2 (a) The unit cell in shear (b) the unit cell with diagonal springs

Once the spring constants are determined, the governing equations of the system can be obtained following the steps below:

1. Write the Lagrangian of the mass spring system as the sum of the kinetic energy of the discrete masses minus the sum of the potential energy of the springs,
2. Derive the equations of motion by applying the principle of least action.

When writing the potential energy of the springs, consider an arbitrarily small displacement of the discrete mass m_i (fig. 3). Assuming the spring deformations are small, the change in length of the edge spring is approximated using a Taylor expansion:

$$\Delta l_i = \sqrt{(l_0 + \Delta l)^2 + \Delta j^2} - l_0 \sim \Delta l + \frac{\Delta j^2}{2l_0} + O(\Delta l^2, \Delta j^2), \quad (i, j) \in \{x, y\} \quad \text{with } i \neq j \quad (5)$$

Since $\Delta l, \Delta j \ll l_0$, $\frac{\Delta j^2}{2l_0} = \frac{\Delta j^2}{2(1 + \frac{\Delta l}{l_0})} \approx 0$

$$\Delta l_i \sim \Delta l + O(\Delta l^2, \Delta j^2), \quad (i, j) \in \{x, y\} \quad \text{with } i \neq j \quad (6)$$

Similarly, the deformation of the diagonal spring is approximated as:

$$\Delta l_d = \sqrt{(x_0 + \Delta x)^2 + (y_0 + \Delta y)^2} - \sqrt{x_0^2 + y_0^2} \sim \frac{x_0 \Delta x + y_0 \Delta y}{\sqrt{x_0^2 + y_0^2}} + O(\Delta x^2, \Delta y^2) \quad (7)$$

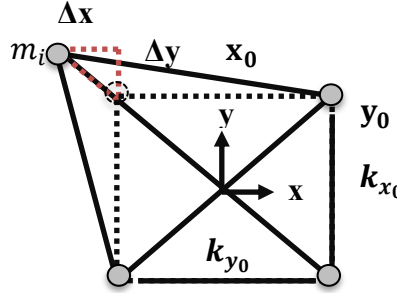


Fig. 3 Arbitrary displacement of a discrete mass in a square unit cell

4. 3-D Mass-spring Models

The 3-D model is a generalization of the 2-D model. The square unit cell is extended to a cubic cell with which three possible spring configurations are investigated. Fig. 4 shows the three elementary configurations of the springs. By combining (a) (b), (a) (c), and (a) (b) (c), the three possible spring configurations are achieved. The configuration (a) (b) is a direct extension of the 2-D case in three dimensional space. Each mass is connected to 18 neighbors. Configuration (a) (c) replaces the face diagonal springs in (a) (b) with body diagonal springs, which reduces the number of connected neighbors of each mass to 14. Configuration (a) (b) (c) is the most complicated spring configuration with each mass connected to 26 neighbors. Trade-off must be made between the effectiveness of the system and the complexity of the spring configuration. Baudet et al. present the analytical expression of the edge spring stiffness (k_x) and the diagonal spring stiffness (k_d) for configuration (a) (c) based on tensile and shearing tests (Baudet et al., 2009):

$$k_x = \frac{Ex_0(4\nu + 1)}{8(1 + \nu)} \quad (8)$$

$$k_d = \frac{3Ex_0}{8(1 + \nu)} \quad (9)$$

Where x_0 is the edge length of the cubic cell, E is the Young's modulus, and ν is the Poisson's ratio. However, modal analysis on a single cubic cell indicates that this configuration is unstable in vibration. Similar observation is also reported by Ladd and Kinney (Ladd and Kinney, 1997) showing that the configuration is unstable to local torsional mode. Consequently the configuration (a) (b) is examined.

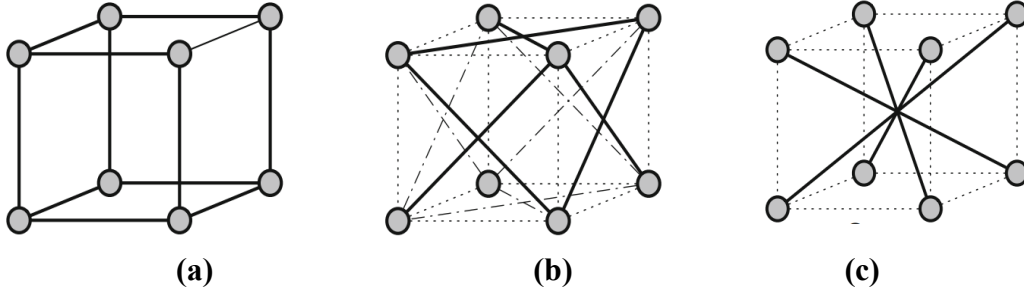


Fig. 4 Elementary spring configurations for 3-D cubic unit cell

By assuming that the elastic material is isotropic and that all the springs have the same stiffness for the configuration (a) (b), the equation of motion can be written (Ladd et al., 1997):

$$\rho \frac{\partial^2 \mathbf{u}}{\partial t^2} = \frac{k}{x_0} (2\nabla(\nabla \cdot \mathbf{u}) + \nabla^2 \mathbf{u}) \quad (9)$$

Where x_0 is the edge length of the cubic cell, k is the stiffness of the springs, \mathbf{u} is the displacement vector of the discrete mass. Based on linear elasticity theory, the equation of motion can be written in terms of the Lamé constants (Landau and Lifshitz, 1986):

$$\rho \frac{\partial^2 \mathbf{u}}{\partial t^2} = \lambda \nabla(\nabla \cdot \mathbf{u}) + \mu(\nabla^2 \mathbf{u} + \nabla(\nabla \cdot \mathbf{u})) \quad (10)$$

By comparing equation (9) and (10), $\lambda = \mu = \frac{k}{x_0}$. Furthermore, the Young's modulus and Poisson's ratio can be expressed in terms of the Lamé constants:

$$E = \frac{\mu(3\lambda + 2\mu)}{\lambda + \mu} = \frac{5k}{2x_0} \quad (11)$$

$$\nu = \frac{\lambda}{2(\lambda + \mu)} = 0.25 \quad (12)$$

The spring stiffness for configuration (a) (b) is thus determined by $k = \frac{2Ex_0}{5}$. The Poisson's ratio is fixed: $\nu = 0.25$. The spring deformations are approximated using Taylor expansion with the small deformation assumption:

$$\Delta_i = \sqrt{(i_0 + \Delta i)^2 + \Delta j^2 + \Delta k^2} - i_0 \sim \frac{i_0 \Delta i + \Delta j + \Delta k}{i_0} + O(\Delta i^2, \Delta j^2, \Delta k^2), \quad i, j, k \in (x, y, z) \quad (13)$$

Since $\Delta i, \Delta j, \Delta k \ll i_0$, $\frac{\Delta j + \Delta k}{i_0} \approx 0$

$$\begin{aligned} \Delta_i &= \sqrt{(i_0 + \Delta i)^2 + \Delta j^2 + \Delta k^2} - i_0 \sim \Delta i + O(\Delta i^2, \Delta j^2, \Delta k^2) \\ \Delta_d &= \sqrt{(x_0 + \Delta x)^2 + (y_0 + \Delta y)^2 + (z_0 + \Delta z)^2} - \sqrt{x_0^2 + y_0^2 + z_0^2} \sim \end{aligned} \quad (14)$$

$$\frac{x_0\Delta x + y_0\Delta y + z_0\Delta z}{\sqrt{x_0^2 + y_0^2 + z_0^2}} + O(\Delta x^2, \Delta y^2, \Delta z^2) \quad (15)$$

As is mentioned in the prior section that the 3-D mass-spring system gives an exact prediction only when the Poisson's ratio $\nu_{3D} = 1/4$. Since the material under study has a Poisson's ratio of 1/3, additional care must be taken. According to Baudet et al. (Baudet et al., 2009), corrective forces can be introduced in addition to springs to account for additional Poisson's effects and thus expand the validity of the mass-spring model as the Poisson's ratio ranges between 0.1 to 0.5. The corrective forces can be introduced in transient dynamics analysis but not in modal analysis in which no forces are considered. The implementation of corrective forces will be explained in details in the future.

5. Model Validation

The aim of this paper is to establish a model that is capable to characterize the dynamics of the built feature at the critical height-to-width ratio in the UAM. Specifically, based on the prior finding that the built feature undergoes resonance at the critical height-to-width ratio, the proposed model should be able to accurately characterize the modal parameters (modal frequencies and mode shapes) of the built feature. Moreover, as an alternative to modeling using finite element method, the mass-spring model should be more computationally favorable. Therefore, the proposed 2-D and 3-D mass-spring systems are implemented to model the built feature. The typical shape of the built feature is a parallelepiped. In the 2-D case, the nominal width of the foil used in UAM is 0.9375 in. (0.0238 m) and the height of the built feature is set to the same value. The UAM accepts a broad range of metals such as aluminum alloys, copper, zinc, nickel, and even titanium. However, aluminum alloy 3003-H18 is selected for its most extensive application in UAM and data availability in the literature. The material properties of aluminum alloy 3003-H18 used in the dynamics model are listed in table 1. Although the built feature is laminated and moderately anisotropic, the influence of anisotropy is small and thus can be neglected. As a result, it is assumed that the material in the built feature is homogeneous and isotropic.

Table 1. The material properties of aluminum alloy 3003-H18

Density (kg/m^3)	Young's Modulus (Pa)	Poisson's ratio
2700	6.9e10	0.33

In the modal analysis, the equations of motion of the mass-spring system are derived first by assembling the element cells:

$$[M]\ddot{\mathbf{x}} + [K]\mathbf{x} = 0$$

Where the mass matrix $[M]$ is diagonal and the stiffness matrix $[K]$ is symmetric and positive definite. Notice that the global mass and stiffness matrices are constructed such that the element matrices are superimposed, meaning that the mass/spring stiffness increases if multiple cells overlap at that position. Then a fixed boundary condition is applied at the bottom of the parallelepiped by deleting rows and columns in $[M]$ and $[K]$ matrices that correspond to nodes at the bottom. By inserting a general solution $\mathbf{x} = \mathbf{X}e^{-\omega t}$ to the system, the eigenvalue problem is formulated:

$$([K] - \omega^2[M])\mathbf{X}e^{-\omega t} = 0$$

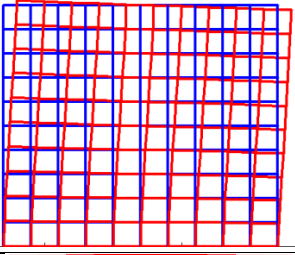
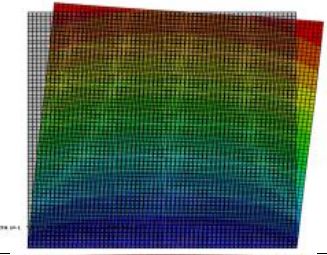
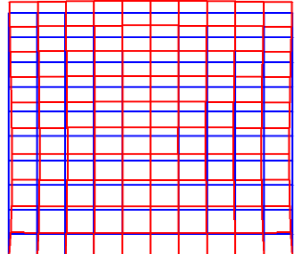
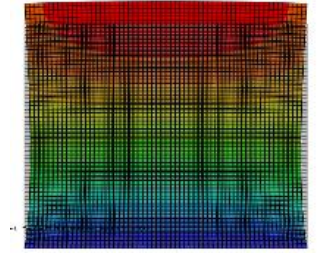
Since $\mathbf{X}e^{-\omega t} \neq 0$,

$$[K] - \omega^2[M] = 0$$

The problem can be readily solved using MATLAB.

The predictions from the mass-spring models are compared with those predicted by finite element models using the commercial software ABAQUS 6-14. Table 2 shows a qualitative comparison of mode shapes predicted by the mass-spring model and the finite element model. The mass-spring model uses a relatively low mesh resolution (10x10) when compared with the mesh of the finite element model (60x60) simply for the purpose of a clear view of the mode shapes. In the mass-spring model, the blue lines represent the undeformed shape and the red ones represent the deformed mode shapes. The mode shapes predicted by the mass-spring model match well with those from the finite element model although the mesh of the mass-spring model is less fine. In addition, a convergence study is performed on both models regarding their predictions of the first five modal frequencies (Table 3). The mass-spring model shows very stable predictions as the mesh resolution increases from 5x5 to 60x60, meaning that the model does not require a highly fine mesh to obtain reliable predictions (fig. 5). The finite element model, however, demonstrates a significant change in predictions as the mesh resolution increases in all but the primary mode (fig. 6). The predictions converge as the mesh resolution reaches 40x40. Moreover, the predictions from a 20x20 mass-spring model are compared with those from a 60x60 finite element model (fig. 7), and the relative error between the two remains within 0.3%. Finally, the two models are compared in terms of CPU time required for solving the problem. The computer in use has an Intel 2.30 GHz double-core processor. The CPU time consumed for solving the 20x20 mass-spring model is 6.9 seconds whereas the time for solving the 60x60 finite element model is 1.6 seconds. It can be concluded that the mass-spring model requires less number of elements than the finite element model does to obtain a similar prediction. However, the computing time of the 2-D mass-spring model is longer than that of the finite element model possibly because the code developed in this work is not as structurally concise and computationally efficient as the code used in the commercial software.

Table 2. Comparison of the mode shapes for the first five modes

Mode number	Mass-spring model (10x10)	Finite element model (60x60)
1		
2		

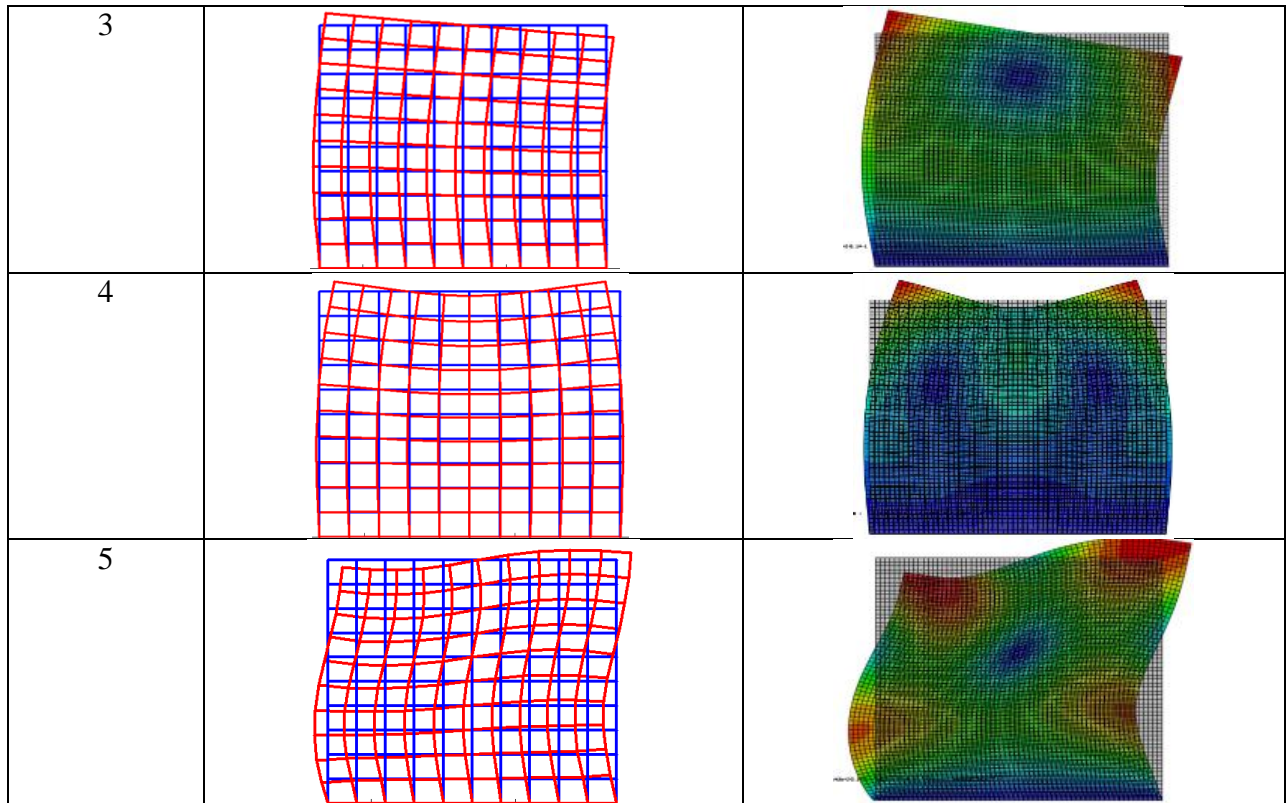


Table 3. Modal frequency predictions with different mesh resolutions in 2-D

Mode number	Mass-spring model (frequency: kHz)				Finite element model (frequency: kHz)			
	5x5	20x20	40x40	60x60	5x5	20x20	40x40	60x60
1	21.16	20.80	20.77	20.76	21.49	22.13	22.15	20.76
2	50.09	50.11	50.10	50.09	24.21	46.94	53.44	50.08
3	55.17	55.80	55.81	55.81	52.72	53.43	59.55	55.82
4	84.62	88.69	88.91	88.94	54.44	59.42	85.79	88.90
5	94.54	95.23	95.19	95.18	56.36	67.60	94.75	95.24

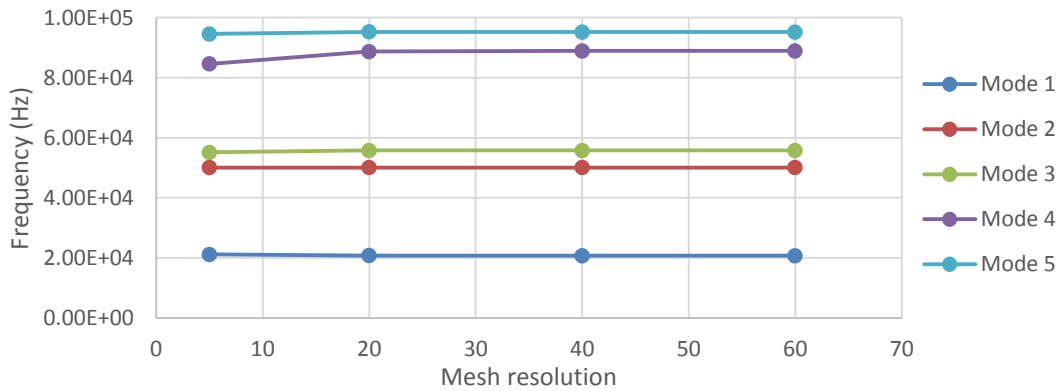


Fig. 5 Convergence of the mass-spring model in 2-D

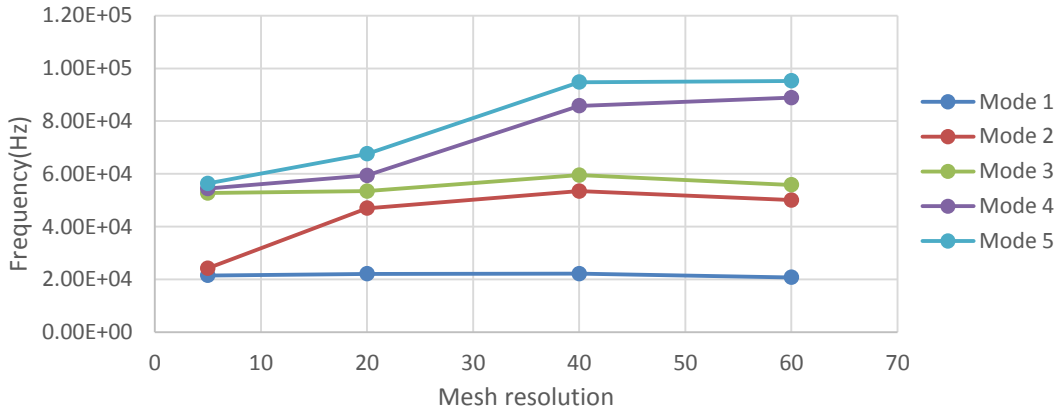


Fig. 6 Convergence of the finite element model in 2-D

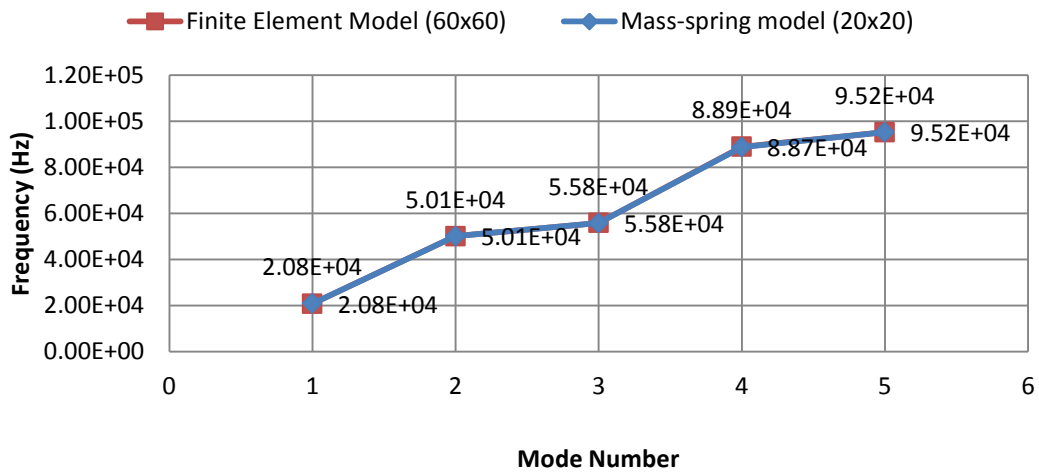


Fig. 7 Modal frequency predictions from 20x20 mass-spring model and 60x60 finite element model in 2-D

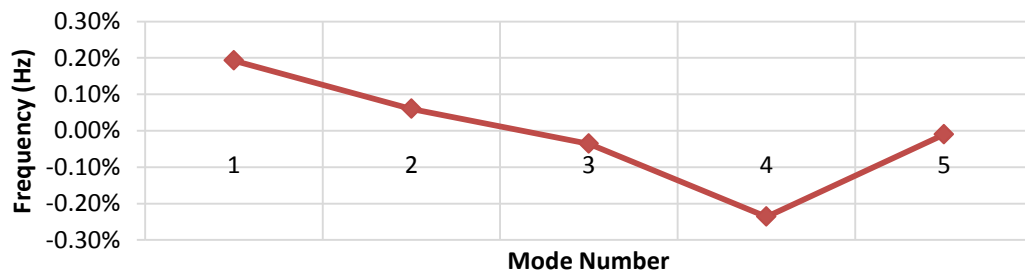
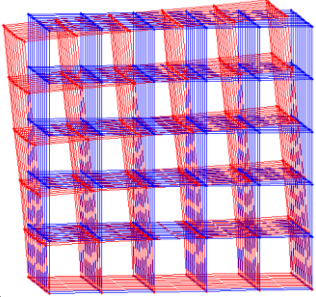
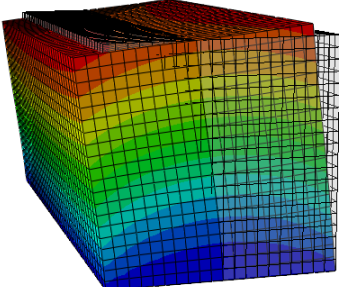
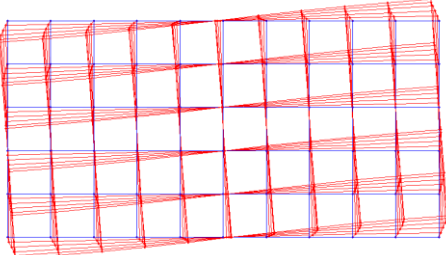
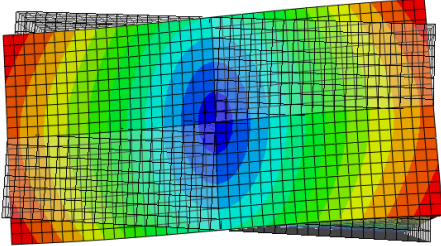


Fig. 8 Relative errors of frequency prediction of 20x20 mass-spring model

For the 3-D case, the geometry of the built feature is set to 0.9375 in. (0.0238 m) in height and width, and 1.875 in. (0.0476 m) in length. The length of the built feature is selected arbitrarily since the height-to-width ratio problem is not sensitive to length (Robinson et al., 2006). The material selected is the same as that in the 2-D case. Table 3 presents a qualitative comparison of the first five mode shapes predicted by the two models. Again, the mass-spring model has a lower mesh resolution (5x5x10) than the finite element model (20x20x40), but this does not undermine its ability to predict the mode shapes. Most of the mode shapes are presented in top view or side view for clarity. Fig.9 and 10 shows the convergence study of the two models in 3-D. Similar to the observations in the 2-D case, the predictions from the mass-spring model show little variance as mesh resolution increases from 3x3x6 to 12x12x24 whereas the predictions in the finite element model undergo radical changes. Specifically, at a mesh resolution of 5x5x10, the finite element model presents multiple “hourglass” mode shapes indicating insufficient mesh refinement and results in five modal frequencies being extremely close to each other. At a mesh resolution of 20x20x40, the predictions from the finite element model start to converge and little variance is found as the mesh is further refined. Notice that the finest mesh for the mass-spring model in the evaluation is only 12x12x24, whereas for the finite element model, it is 30x30x60. Fig. 11 shows a comparison of the modal frequency prediction from a 3x3x6 mass-spring model and a 30x30x60 finite element model. The relative error of the prediction from the two models lies within 5% (fig. 12). In terms of computational cost, the CPU time for computing for the 3x3x6 mass-spring model is only 1.01 seconds, whereas the time for the 30x30x60 finite element model is 6.2 seconds. This is probably due to the fact that the mesh resolution rather than the conciseness of the code starts to constrain the computing time as the model changes from 2-D to 3-D. Consequently, the 3-D mass-spring model requires a much lower mesh resolution and thus less computation time than the 3-D finite element model does to obtain a reliable prediction.

Table 4. Comparison of the mode shapes for the first five modes

Mode number	Mass-spring model (5x5x10)	Finite element model (20x20x40)
1		
2		

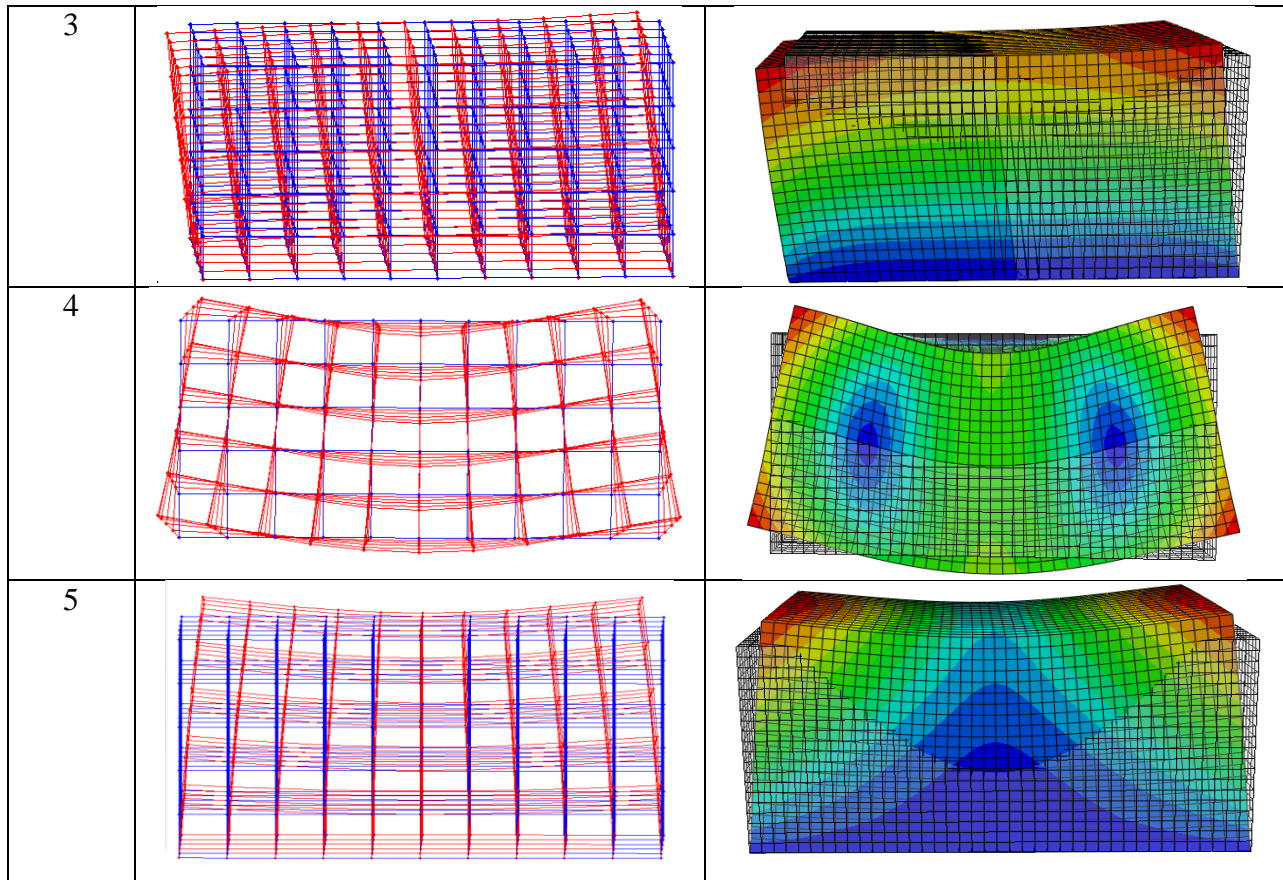


Table 5 Modal frequency predictions with different mesh resolutions in 3-D

Mode number	Mass-spring Model (Frequency: kHz)				Finite Element Model (Frequency: kHz)			
	3x3x6	5x5x10	10x10x20	12x12x24	5x5x10	10x10x20	20x20x40	30x30x60
1	22.8	22.4	22.2	22.1	20.3	22.6	22.7	22.7
2	27.5	27.4	27.3	27.3	20.4	27.9	28.0	28.1
3	28.5	27.9	27.4	27.4	20.5	28.1	28.1	28.1
4	44.6	45.1	45.1	45.1	20.7	41.3	46.0	46.1
5	49.2	50.2	50.5	50.5	20.7	41.3	51.8	51.8

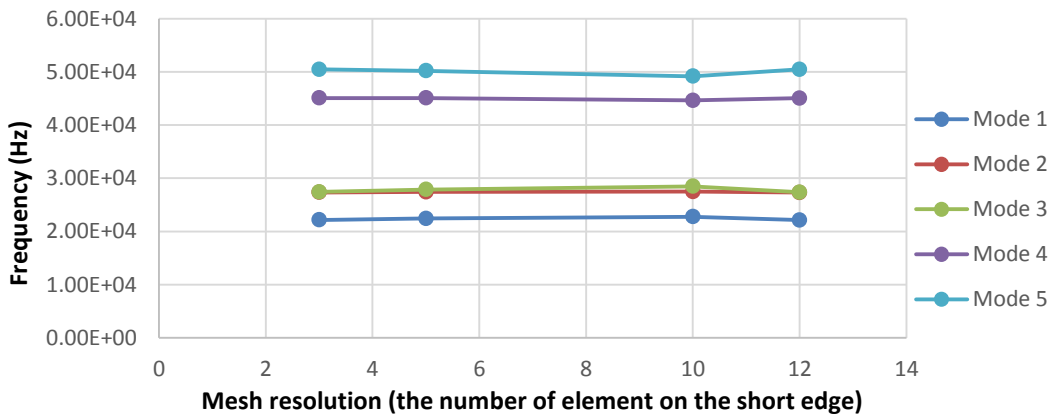


Fig. 9 Convergence of the mass-spring model in 3-D

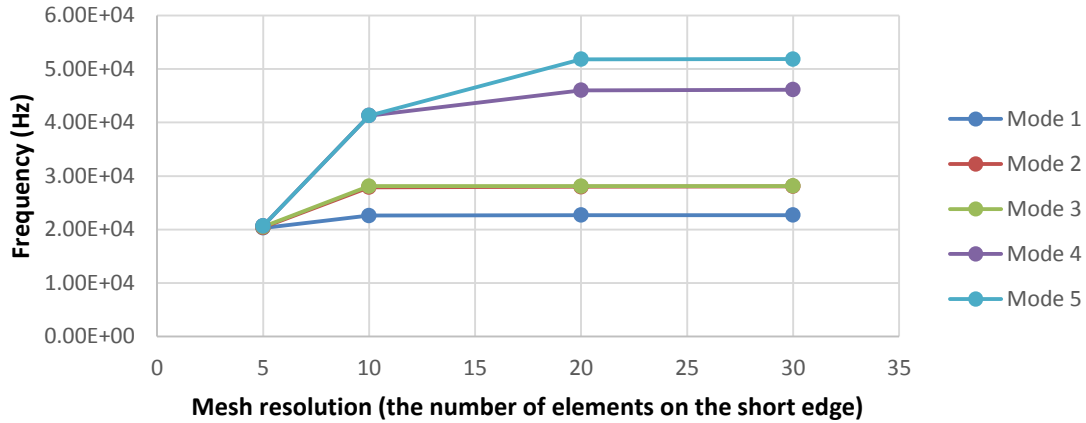


Fig. 10 Convergence of the finite element model in 3-D

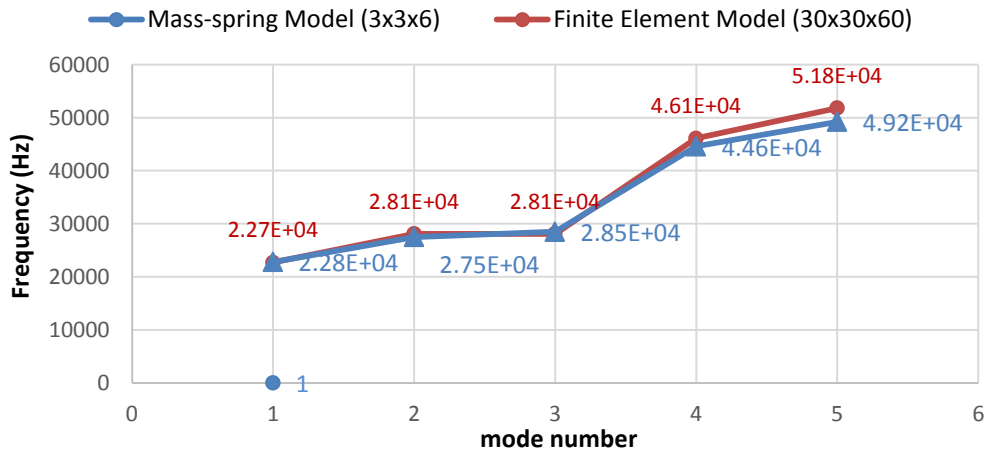


Fig. 11 Modal frequency predictions from 20x20 mass-spring model and 60x60 finite element model in 3-D

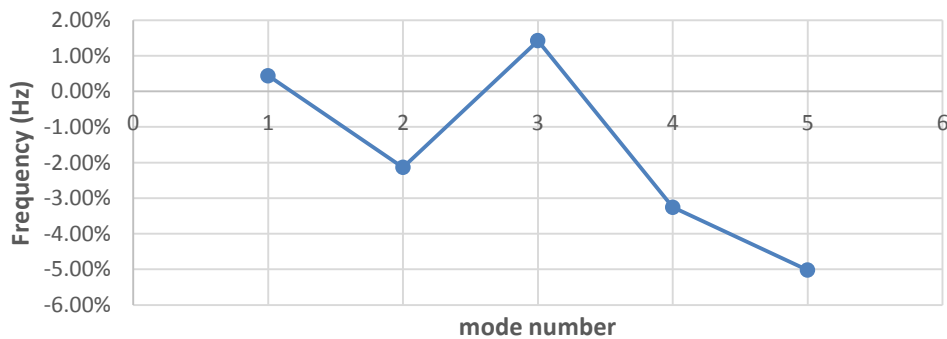


Fig. 12 Relative errors of frequency prediction of 20x20 mass-spring model

6. Conclusion and future work

In summary, lumped parameter models consisting of mass-spring networks in 2-D and 3-D are proposed to characterize the dynamics of the built feature in UAM. The mass-spring models are validated by comparing their modal predictions with those from 2-D and 3-D finite element models. It is shown that the mass-spring models require much less number of elements than the finite element model in predicting the modal parameters with similar accuracy. The computational cost of the mass-spring model is much lower than that of the finite element model only in the 3-D case possibly due to the fact that in the 2-D case the computational cost from a refined mesh is small and has less influence on the overall computing time. From preliminary analysis, the mass-spring model proves to be computationally efficient and effective in characterizing the dynamics of the built feature in UAM. The next immediate step is to introduce an elasto-plastic bonding layer on top of the mass-spring structure. By examining the deformation of the bonding layer under the combined effects of the excitation of the sonotrode and the resonance of the built feature, the bond failure due to geometry change of the built feature will be better understood and quantified in the future.

References

- Baudet, Vincent, et al. "Integrating tensile parameters in hexahedral mass-spring system for simulation." (2009)
- Born, M., & Huang, K. (1954). Dynamical theory of crystal lattices
- Born, M., Ann. Physik 44, 605 (1914)
- Cosby, J. A. (2013). *Development of 2D to 3D FEA Conversion Factors for Natural Frequencies of Beams Under Transverse Vibrations* (Doctoral dissertation, Rensselaer Polytechnic Institute).
- De Vries, E. (2004). *Mechanics and mechanisms of ultrasonic metal welding*.
- Gibert, J. M., Austin, E. M., & Fadel, G. (2010). Effect of height to width ratio on the dynamics of ultrasonic consolidation. *Rapid Prototyping Journal*, 16(4), 284–294. doi:10.1108/13552541011049306
- Gibert, J. M., McCullough, D. T., Fadel, G. M., Martin, G. K., & Austin, E. M. (2009, January). Stick-slip dynamics in ultrasonic consolidation. In ASME 2009 International Design Engineering Technical Conferences and Computers and Information in Engineering Conference (pp. 307-317). American Society of Mechanical Engineers.
- Kot, M., Nagahashi, H., & Szymczak, P. (2014). Elastic moduli of simple mass spring models. *The Visual Computer*, 1-12.
- Ladd, A. J., & Kinney, J. H. (1997). Elastic constants of cellular structures. *Physica A: Statistical Mechanics and its Applications*, 240(1), 349-360.

Landau, L. D., & Lifshitz, E. M. (1986). Theory of Elasticity, vol. 7. *Course of Theoretical Physics*, 3, 109.

Lloyd, B. A., Kirac, S., Székely, G., & Harders, M. (2008). Identification of dynamic mass spring parameters for deformable body simulation. *The Eurographics Association*.
Nealen, Muller, Keiser, Boerman, and Carlson. "Physically based deformable models in computer graphics." *Computer Graphics Forum*. Vol. 25. No. 4. Blackwell Publishing Ltd, 2006.

Louchet, J., Provot, X., & Crochemore, D. (1995). *Evolutionary identification of cloth animation models* (pp. 44-54). Springer Vienna.

Ram, G. D. J., Robinson, C., Yang, Y., & Stucker, B. E. (2007). Use of ultrasonic consolidation for fabrication of multi-material structures. *Rapid Prototyping Journal*, 13(4), 226–235.
doi:10.1108/13552540710776179

Rice, J.R., "Mechanics of Solids", section of the article on "Mechanics", in *Encyclopaedia Britannica* (1993 printing of the 15th edition), volume 23, pp. 734- 747 and 773, (1993).

Robinson, C. J., Zhang, C., Ram, G. J., Siggard, E. J., Stucker, B., & Li, L. (2006, August). Maximum height to width ratio of freestanding structures built using ultrasonic consolidation. In *Proceedings of the 17th solid freeform fabrication symposium, Austin, Texas, USA, August*.

San-Vicente, G., Aguinaga, I., & Celiğüeta, J. T. (2012). Cubical mass-spring model design based on a tensile deformation test and nonlinear material model. *Visualization and Computer Graphics*, IEEE Transactions on, 18(2), 228-241.

Zhang, C., & Li, L. (2008). A friction-based finite element analysis of ultrasonic consolidation. *Welding Journal-New York-*, 87(7), 187.

Zhang, C., Zhu, X., & Li, L. (2006, October). A study of friction behavior in ultrasonic welding (consolidation) of aluminum. In *Proceedings of the AWS Conference* (pp. 151-156).